

Investigation of the Effect of the In-Cylinder Tumble Motion on Cycle-to-Cycle Variations in a Direct Injection Spark Ignition (DISI) Engine Using Large Eddy Simulation (LES)

Wei Li¹ · Yufeng Li² · Tianyou Wang¹ · Ming Jia³ ·
Zhizhao Che¹ · Daming Liu¹

Received: 11 October 2015 / Accepted: 13 September 2016 / Published online: 28 September 2016
© Springer Science+Business Media Dordrecht 2016

Abstract Cycle-to-cycle variations (CCVs) limit the extension of the operating range by inducing load variations and even misfire and/or knock for direct injection spark ignition (DISI) engines and hence need to be controlled. One of the effective and flexible ways to reduce CCV is to employ a charge motion control valve. This study is aimed to analyze the flow characteristics and CCV using large eddy simulation (LES) and fast Fourier transform (FFT) in a non-reacting, DISI engine equipped with a tumble flap (i.e., a specific type of charge motion control valve) inside the intake port. The in-cylinder flow characteristics are analyzed in detail, and the possible effects of multi-scale structures of the fluid field on the subsequent ignition and combustion processes are also discussed. Computational results indicate that closing the tumble flap helps enhance the intensity of the coherent structures and increase the total integral length scale (ILS) while decreasing the Kolmogorov scale and stabilizing the flow field by suppressing the CCV of tumble ratio and tumble center. Furthermore, based on a newly developed FFT triple decomposition, each instantaneous flow field is decomposed into three subfields, termed ensemble mean part and low- and high-spatial frequency parts, respectively. It is found that switching the tumble flap position greatly affects the first two subfields, but it has negligible effect on the last part. With the closed tumble flap, the energy portion of the mean part increases, the rate of energy decay reduces, and the CCV of the low- and high-spatial frequency parts decreases.

Keywords In-cylinder tumble flow · Integral length scale · Large eddy simulation · Fast fourier transform · Cycle-to-cycle variations · Charge motion control valve

✉ Tianyou Wang
wangtianyou@tju.edu.cn

¹ State Key Laboratory of Engines, Tianjin University, No. 92, Weijin Road, Nankai District, Tianjin, China

² Combustion Process Research Department, China North Engine Research Institute, Datong, China

³ School of Energy and Power Engineering, Dalian University of Technology, Dalian, China

1 Introduction

The ideal working condition in internal combustion (IC) engines is that the events of air motion and combustion are consistent from cycle to cycle. However, cycle-to-cycle variations (CCVs) (also refer to cyclic variations) are unavoidable in practical IC engines. CCV needs to be controlled effectively in direct injection spark ignition (DISI) engines at low load and speed conditions in order to realize stable combustion [1]. The primary cause of the CCV in IC engines is the variations of the flow field structures, as indicated by Young [2] and Ozdor et al. [3]. In particular, the unstable coherent structures of the flow field contain most of the fluctuating energy and may play a dominant role in triggering the cyclic variations [4]. Therefore, a comprehensive understanding of the in-cylinder flow characteristics is important to monitor and control the CCV of DISI engines.

As a large-scale organized flow with its rotation plane perpendicular to the cylinder axis, tumble flow employed in DISI engines is not only to transport the fuel towards the spark plug for charge stratification at partial loads but also to accelerate the burning rate with small CCV at full loads [5]. Tumble flow has been studied in the last two decades in spark ignition (SI) engines using methods including hot wire anemometry (HWA) [6], laser Doppler velocimetry (LDV) [7, 8], particle tracking velocimetry (PTV) [9], particle image velocimetry (PIV) [10, 11], and computational fluid dynamic (CFD) simulations [12, 13]. Many aspects of the tumble flow have been studied previously, such as the instantaneous and bulk velocities, the vorticity and strain rates, the formation and decay of the tumble motion, the turbulence intensities and integral length scale (ILS), and the potential effect of the tumble flow on the following spray and combustion.

As an estimation of the size of the largest turbulent eddies containing most of the turbulence kinetic energy, the features of ILS have been investigated in several studies [8, 10, 11, 14, 15]. In many of these works, ILS was indirectly calculated based on Taylor's hypothesis [7], which is used to relate the time scales to the length scales. However, Taylor's hypothesis is only valid in homogeneous and stationary turbulent flows; thus, the estimation of the in-cylinder ILS based on Taylor's hypothesis is still questionable. Direct measurements of ILS by integrating the spatial autocorrelation function were performed using the multi-point LDV and PIV measurements. Li et al. [11, 16] carried out a series of studies on the estimation of the in-cylinder ILS. The results showed that ILS varied not only over the flow field but also when different components of the total fluctuating velocity were employed. In addition, the distribution of ILS corresponding to the four different components showed no similar features or regular behaviors, indicating that the turbulent flow was highly anisotropic. However, Heim and Ghandhi [10] performed a study on the ILS in the swirl plane at four engine speeds and eight engine configurations and found that the swirl flow was highly isotropic because the horizontal ILS agreed well with the vertical one.

To realize the designed in-cylinder tumble motion, various kinds of charge motion control valves have been employed near the intake valves [17, 18] or far away from the intake ports [19–23]. Fischer et al. [19] investigated the CCV in an optical stratified-charge gasoline direct injection (GDI) engine with variable tumble systems using PIV, spark emission spectroscopy, and high-speed flame visualization. It was found that a suitable inlet flow condition improved the flow stability during the compression stroke and further decreased the fluctuation range of air–fuel ratio in the spark plug gap. The center and propagation of the flame kept nearly unchanged from 1 cycle to another. Vu and Guibert [23] performed an experimental study to assess the influence of a flap inserted upstream the inlet valve on the CCV in a two-valve SI engine with a pent roof using proper orthogonal decomposition

(POD). It was confirmed that the flap insertion depth inside the inlet pipe significantly affected the in-cylinder cyclic variations. Despite significant advances in experimental techniques in recent years [24], the posteriori analyses are still difficult to be applied to IC engines [13].

With the development of CFD techniques, large eddy simulation (LES) has been increasingly used for the design of advanced IC engines because it can satisfy the requirements of computational efficiency and accuracy simultaneously compared with Reynolds-averaged Navier–Stokes (RANS) and direct numerical simulation (DNS) [25]. Recently, many studies have been focused on studying the cycle-to-cycle velocity fluctuations and their impact on the spray and mixing processes in realistic engine configurations based on LES [26–28]. To validate the predictions of LES, a measured velocity field from 25 cycles was employed, and the results indicated that the multi-cycle LES was capable of capturing the transient in-cylinder turbulence characteristics, and the predicted CCV of the flow field was consistent with the PIV measurements [29]. Analysis of the comparison between the experimental measurements and LES predictions of 50-cycle velocity field was carried out by Baumann et al. [12] in the same engine configuration as in Ref. [29], and it was found that LES can predict well the mean and root-mean-square (RMS) flow velocities. The LES calculation with a relatively coarse mesh could capture the most significant fluid dynamics at a length scale larger than the filter size in the cylinder.

To further understand the CCV of the flow field, the instantaneous in-cylinder velocity field is often decomposed into three parts, named the mean part, the low-frequency part referred to as the coherent part, and the high-frequency part equivalent to the incoherent turbulent part [30]. As a widely used spatial filtering technique, fast Fourier transform (FFT) has been introduced to separate the coherent and incoherent parts [11, 14, 31, 32]. However, Joo et al. [31] concluded that it was difficult to determine the cutoff length (or the cutoff frequency) in the FFT calculation for different experimental conditions. Meanwhile, the results varied significantly with the selection of the cutoff length. POD was first introduced by Lumley [33] in 1967 and has been used to identify the coherent structure and evaluate the CCV of the in-cylinder turbulent flow in recent years [34–37]. Nevertheless, POD still faced the challenge to choose the POD mode number as indicated by Roudnitzky et al. [38] because POD was also based on the Fourier decomposition. They thought that it was challenging to make an objective determination of the separation mode number at different crank angles in engine simulations.

At present, the characteristics of the large- and small-scale flow structures, the corresponding fluctuations, and ILS in realistic engine geometries equipped with charge motion control valve have not been well understood, especially the tumble features. Moreover, it is necessary to find an objective criterion to decompose the velocity field into three subfields and further evaluate the effect of charge motion control valve on the in-cylinder flow dynamics and cyclic variations associated with each subfield contribution.

In the present work, a LES without spray or combustion was conducted in a realistic DISI engine configuration with a tumble flap (i.e., a specific type of charge motion control valve). First, the effect of the tumble flap on the in-cylinder aerodynamics was analyzed through the velocity fluctuation intensity and the multi-scale structures. For a comprehensive evaluation of the influence of the tumble flap on the cyclic variations, a newly developed two-dimensional (2D) FFT triple decomposition with the spatially averaged ILS as the cutoff length was further performed based on the LES data to quantify the CCV of the in-cylinder turbulent flow.

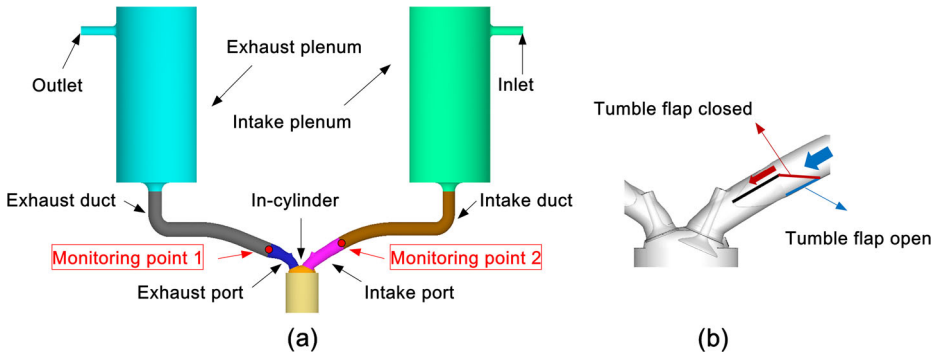


Fig. 1 Geometric configuration and schematic of the tumble flap

2 Geometric Configuration

This paper focuses on the flow field in a four-valve, four-stroke DISI engine with a pent roof combustion chamber and a tumble flap. Figure 1a shows the geometric configuration, which was generally employed in the investigations of transparent combustion chamber (TCC) engines [34], and Fig. 1b shows the schematic plot of the tumble flap used to control the in-cylinder tumble intensity. The closed tumble flap makes the in-cylinder air developed into a stronger tumble flow compared with the open tumble flap. The detailed description of the advantages of employing the tumble flap can be found in Ref. [39]. The geometric dimensions of the main components in the configuration are listed in Table 1, and the engine specifications and valve timings of the test engine are summarized in Table 2. In this study, zero crank angle degree ($^{\circ}\text{CA}$) refers to the top dead center (TDC) at the beginning of the intake stroke.

The tumble plane shown in Fig. 2 is chosen for data analysis. The location of the grid points between any two crank angles is different from each other, resulting from the dynamic mesh, and the interpolation procedure is thus necessary prior to performing data analysis.

3 Computational Setup

The commercial three-dimensional (3D) CFD code, CONVERGE [40], is employed to simulate the cyclic variations of the engine flow. It is capable of automatically generating the

Table 1 Intake and exhaust geometries

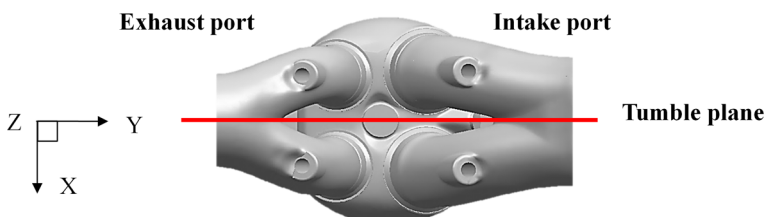
Component	Diameter (mm)	Length (mm)
Inlet	20.0	82.0
Intake plenum	200.0	400.0
Intake duct	39.0	394.6
Outlet	20.0	82.0
Exhaust plenum	200.0	400.0
Exhaust duct	33.4	382.2

Table 2 Engine specifications and valve timings

Parameter name	Parameter value
Bore	82.5 mm
Stroke	86 mm
Connecting rod length	168 mm
Geometric compression ratio	9.7:1
TDC clearance height	1.4 mm
Intake valve opening	714°CA
Intake valve maximum lift	127°CA
Intake valve closing	262°CA
Exhaust valve opening	432°CA
Exhaust valve maximum lift	609°CA
Exhaust valve closing	7°CA
Engine speed	800 rev min ⁻¹

real-time and high-quality orthogonal hexahedral meshes. Meanwhile, the technology of adaptive mesh refinement (AMR) is employed to automatically refine the grid based on the flow. AMR can realize the local grid refinement and hence is helpful to improve the grid resolution with relatively low computational cost. The LES model used in this study is the one-equation eddy viscosity model [41]. To reduce the computational cost in the near-wall regions, the Werner and Wengle [42] wall model is introduced. The grid control strategy of fixed embedding (see Fig. 3) is used to realize the balance between computational efficiency and accuracy. Goryntsev et al. [43] found that the mesh size about 1 mm in the cylinder was the minimum requirement to obtain reliable results. Therefore, the size of the base cell in the two plenums is 8 mm, the size of most of the in-cylinder cells is 1 mm, and the finest meshes of 0.5 mm are used in valve regions. In the near-wall region of the intake and exhaust ducts and the intake and exhaust plenums, bound embedding used by Yang et al. [44] and Kuo et al. [45] is employed here. The total number of cells in the whole computational domain is about 1,000,000 at bottom dead center (BDC) and approximately 700,000 at TDC.

The working fluid is compressible air, which is solved according to a Redlich–Kwong equation of state. The temperature of the wall in all regions is fixed at 320 K, and the initial gas temperature is 318.2 K. As for the pressure settings, the initial pressures in the exhaust port, the exhaust duct, and the exhaust plenum are set to be 96,300 Pa, while the pressure in the rest of regions is set to be 101,325 Pa. Moreover, the non-slip boundary condition is employed for all geometric surfaces except for the intake plenum inlet and exhaust plenum

**Fig. 2** Coordinate system and tumble plane schematic

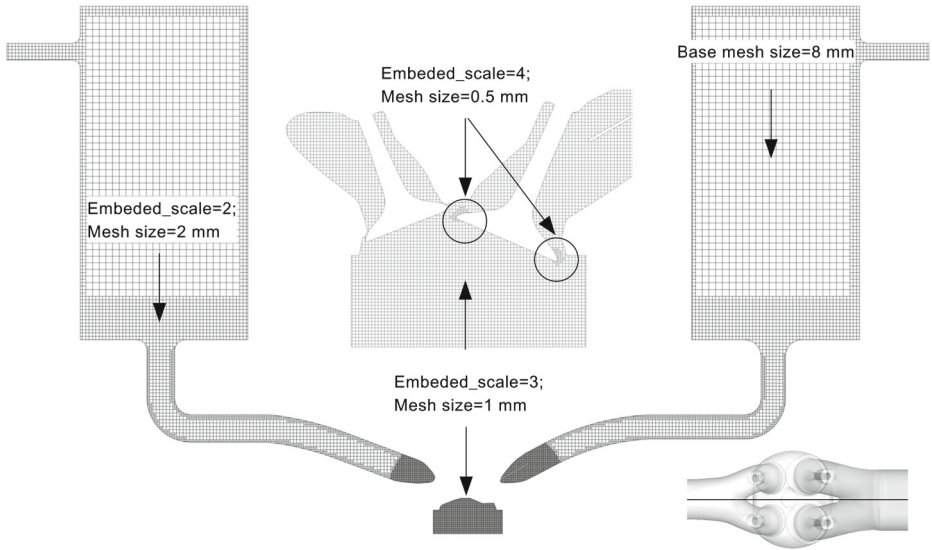


Fig. 3 Computational mesh for the simulation of the DISI engine

outlet. In order to obtain the boundary conditions for the inlet and the outlet, a detailed one-dimensional (1D) flow model in GT-Power is employed to obtain the time-varying pressure and temperature information.

Two cases with the open and closed tumble flaps are modeled, which are referred to hereafter as low tumble ratio case (LTRC) and high tumble ratio case (HTRC), respectively. A simulation of 70 consecutive engine cycles is carried out, and the results of the first 10 cycles are discarded in the analysis of the computational results. More details can be found in Ref. [39].

4 Calculation of Flow Parameters

4.1 Mean velocity and low- and high-frequency fluctuating velocities

Because of the high speed and transient characteristics of the in-cylinder flow, the flow characteristics with large-scale structures in engines cannot be effectively studied using the traditional phase-averaging procedure due to the periodically changing boundary conditions caused by the piston and valve motion. It is generally accepted that the instantaneous velocity can be decomposed into three components [11, 32, 38, 46], through which the reasons for CCV can be recognized.

A 2D transient velocity ($\vec{U}_{(\theta,y,z,i)}$) at the (y, z) grid node in the i th cycle at crank angle θ can be decomposed into three distinct parts including an ensemble mean part ($\vec{U}_{EA(\theta,y,z)}$), a low-spatial frequency (large-scale or the coherent) part ($\vec{u}_{LF(\theta,y,z,i,\lambda)}$), and a high-spatial frequency (small-scale or incoherent) part ($\vec{u}_{HF(\theta,y,z,i,\lambda)}$) as

$$\vec{U}_{(\theta,y,z,i)} = \vec{U}_{EA(\theta,y,z)} + \vec{u}_{F(\theta,y,z,i)} \tag{1}$$

with

$$\vec{u}_{F(\theta,y,z,i)} = \vec{u}_{LF(\theta,y,z,i,\lambda)} + \vec{u}_{HF(\theta,y,z,i,\lambda)} \tag{2}$$

where \vec{u}_{LF} and \vec{u}_{HF} are the function of the cutoff length (λ). The ensemble-averaged mean velocity ($\vec{U}_{EA(\theta,y,z)}$) can be computed based on the mean of the instantaneous velocity values as

$$\vec{U}_{EA(\theta,y,z,i)} = \frac{1}{N} \sum_{i=1}^N \vec{U}_{(\theta,y,z,i)} \tag{3}$$

where N is the number of engine cycles (60 in this study).

For the triple decomposition of the velocity field, a 2D spatial filtering technique based on FFT is used to separate the low- and high-frequency velocity fluctuations from the total flow field. The major drawback of the triple decomposition of the velocity field based on FFT is the uncertainties in determining the cutoff length (λ). It is worth mentioning that λ is determined based on the spatially averaged ILS for the first time in this paper according to the fact that the scale of the turbulent eddies is generally close to the low-frequency part estimated by ILS.

$\vec{U}_{(\theta,y,z,i)}$ is first transformed into the spatial frequency domain using 2D FFT, and then the 2D spectrum is multiplied by a Fermi–Dirac soft cutoff filter [8] as follows:

$$\frac{1}{1 + \exp((\kappa_{yz} - \kappa_c)/(0.1\kappa_c))} \tag{4}$$

where κ_{yz} is the 2D wavenumber expressed as

$$\kappa_{yz} = \sqrt{\kappa_y^2 + \kappa_z^2} \tag{5}$$

where κ_y and κ_z correspond respectively to the Y -component and Z -component of the spectrum field and κ_c is the cutoff wavenumber defined as

$$\kappa_c = \frac{2\pi}{\lambda} \tag{6}$$

The Fourier coefficients gradually reduce from above κ_c to zero during the filter process. Finally, a 2D inverse FFT is performed on the processed Fourier coefficients, and a low-pass and spatially averaged velocity field is obtained accordingly. The low-frequency (large-scale) part ($\vec{u}_{LF(\theta,y,z,i,\lambda)}$) can then be obtained by subtracting the spatially ensemble-averaged velocity ($\vec{U}_{EA(\theta,y,z)}$) from the inverse FFT results, while the high-frequency (small-scale) fluctuating velocity ($\vec{u}_{HF(\theta,y,z,i,\lambda)}$) is calculated according to Eqs. 1 and 2.

4.2 Velocity fluctuation kinetic energy

The ensemble-averaged total velocity fluctuation kinetic energy is derived from the total velocity fluctuation intensity [11] as

$$E_{F,EA(\theta,y,z)} = \frac{1}{2} \left(v_{F,EA(\theta,y,z)}^2 + w_{F,EA(\theta,y,z)}^2 \right) \tag{7}$$

where $v'_{F,EA(\theta,y,z)}$ and $w'_{F,EA(\theta,y,z)}$ are the total velocity fluctuation intensities in the y - and z -coordinates, respectively, which are calculated based on the RMS of the total fluctuating velocity of components. To be specific, the instantaneous Y -component and Z -component

of the total fluctuating velocity ($\vec{u}'_{F(\theta,y,z,i)}$) are $v_{F(\theta,y,z,i)}$ and $w_{F(\theta,y,z,i)}$, respectively. The RMS value of $v_{F(\theta,y,z,i)}$ represented by $v'_{F,EA(\theta,y,z,i)}$ is defined as

$$v'_{F,EA(\theta,y,z)} = \sqrt{\frac{1}{N} \sum_{i=1}^N v_{F(\theta,y,z,i)}^2} \tag{8}$$

and the total RMS value of $\vec{u}'_{F(\theta,y,z,i)}$ in both the Y - and Z -components is given by

$$vw'_{F,EA(\theta,y,z)} = \sqrt{v_{F(\theta,y,z)}^2 + w_{F(\theta,y,z)}^2} \tag{9}$$

The spatial average of the ensemble-averaged total fluctuating kinetic energy is described as

$$E_{F,EA,SA(\theta)} = \frac{1}{N_{g(\theta)}} \sum_{(y,z)} E_{F,EA(\theta,y,z)} \tag{10}$$

where $N_{g(\theta)}$ is the total grid points in each velocity field at a specific crank angle.

Once the total fluctuating velocity ($v_{F(\theta,y,z,i)}$) is replaced by the large-scale or small-scale fluctuating velocity, the large-scale or small-scale velocity fluctuation intensity (i.e., $v'_{LF,EA(\theta,y,z,\lambda)}$ or $v'_{HF,EA(\theta,y,z,\lambda)}$) can be obtained. In addition, the spatial average of the ensemble large-scale or small-scale fluctuation kinetic energy (i.e., $E_{LF,EA,SA(\theta,\lambda)}$ or $E_{HF,EA,SA(\theta,\lambda)}$) can also be determined accordingly.

4.3 CCV of low- and high-frequency fluctuating velocities

To investigate the evolution of the CCV, the standard deviation of the instantaneous fluctuating velocity, which quantifies the fluctuation of the RMS about the average, is calculated as follows:

$$\sigma_{v_{LF}(\theta)} = \sqrt{\frac{\sum_{i=1}^N \left[|v_{LF(\theta,y,z,i,\lambda)}| - v'_{LF,EA(\theta,y,z,i,\lambda)} \right]^2}{N - 1}} \tag{11}$$

$$\sigma_{v_{HF}(\theta)} = \sqrt{\frac{\sum_{i=1}^N \left[|v_{HF(\theta,y,z,i,\lambda)}| - v'_{HF,EA(\theta,y,z,i,\lambda)} \right]^2}{N - 1}} \tag{12}$$

where $\sigma_{v_{LF}(\theta)}$ and $\sigma_{v_{HF}(\theta)}$ can be used to quantify the CCV of the large- and small-scale fluctuating velocity fields along the y -axis at each crank angle [31]. The definitions and equations for the Z -component fluctuating velocity are the same as those of the Y -component except that $v_{LF(\theta,y,z,i,\lambda)}$ and $v_{HF(\theta,y,z,i,\lambda)}$ are replaced by $w_{LF(\theta,y,z,i,\lambda)}$ and $w_{HF(\theta,y,z,i,\lambda)}$, respectively.

4.4 Tumble ratio

The spatially averaged tumble ratio (TR) in the x -direction at θ° CA in cycle i is defined as the ratio of the angular speed of the flow about the mass center (ω_x) to the angular speed of the crankshaft (ω_c) as [11]

$$TR_{x(\theta,i)} = \frac{\omega_x}{\omega_c} = \frac{\sum_{(y,z)} \vec{r}'_{(\theta,y,z,i)} \times \vec{u}'_{(\theta,y,z,i)}}{\omega_c \sum_{(y,z)} \vec{r}'_{(\theta,y,z,i)} \cdot \vec{r}'_{(\theta,y,z,i)}} \tag{13}$$

where ω_x can be obtained by dividing the angular momentum (L_x) by the moment of inertia ($I_{[x]}$) as

$$\omega_x = \frac{L_x}{I_{[x]}} \tag{14}$$

For a discrete system of cells, the angular momentum about the x -axis (L_x) can be calculated as

$$L_x = \sum_{n=1}^{N_g(\theta)} m_n ((y_n - y_{cm})w_n - (z_n - z_{cm})v_n) \tag{15}$$

where m_n is the mass of each cell, y_n and z_n are the coordinates of each cell, v_n and w_n are respectively the velocity components for each cell in the y and z -coordinates, and y_{cm} and z_{cm} represent the location of the mass center.

The moment of inertia about the x -axis (I_x) for a system of cells can be expressed as

$$I_x = \sum_{n=1}^{N_g(\theta)} m_n [(y_n - y_{cm})^2 + (z_n - z_{cm})^2] \tag{16}$$

The spatially averaged TR in the y - and z -directions at θ° CA in cycle i is defined in the same way as above.

4.5 Integral length scale and turbulent Reynolds number

The ILS along the y -axis and z -axis can be calculated by the integral of the spatial autocorrelation coefficient of the total fluctuating velocities in the correlation plane (ζ, η). The ILS of a 2D velocity field have four 1D components, viz., $L_{yy}, L_{zy}, L_{yz},$ and L_{zz} , where the first subscript stands for the integral velocity component and the second subscript represents the direction of the integral. The ILS components L_{yy} and L_{zz} are taken, for example, to describe the calculation process of ILS, and the other two ILS components can be obtained in the same way [11, 47].

$$L_{yy}(\theta, y, z) = \int_0^{\Delta y_{max}} R_{y(\theta, y, z, \xi, 0)} d\xi \tag{17}$$

$$L_{zz}(\theta, y, z) = \int_0^{\Delta z_{max}} R_{z(\theta, y, z, 0, \eta)} d\eta \tag{18}$$

where the upper limits of the integral (i.e., Δy_{max} and Δz_{max}) are the geometric dimensioning along the y -axis and z -axis, where the correlation coefficient is zero for the first time. In addition, the spatial autocorrelation functions of the total fluctuating velocity of components at point (y, z) , $R_{y(\theta, y, z, \xi, 0)}$ and $R_{z(\theta, y, z, 0, \eta)}$, are given by

$$R_{y(\theta, y, z, \xi, 0)} = \frac{\frac{1}{N} \sum_{i=1}^N v_{F(\theta, y, z, i)} \cdot v_{F(\theta, y+\xi, z, i)}}{v'_{FEA(\theta, y, z)} \cdot v'_{FEA(\theta, y+\xi, z)}} \tag{19}$$

$$R_{z(\theta, y, z, 0, \eta)} = \frac{\frac{1}{N} \sum_{i=1}^N w_{F(\theta, y, z, i)} \cdot w_{F(\theta, y, z+\eta, i)}}{w'_{FEA(\theta, y, z)} \cdot w'_{FEA(\theta, y, z+\eta)}} \tag{20}$$

In addition, the total ILS in the Y - and Z -coordinates denoted as L_y and L_z can be calculated as follows:

$$L_{y(\theta,y,z)} = \sqrt{L_{yy(\theta,y,z)}^2 + L_{zy(\theta,y,z)}^2} \quad (21)$$

$$L_{z(\theta,y,z)} = \sqrt{L_{yz(\theta,y,z)}^2 + L_{zz(\theta,y,z)}^2} \quad (22)$$

The detailed calculation process of ILS is as follows. Because the velocity field is not a regular rectangular region in the combustion chamber, the location of the first velocity data point is different at different crank angles. Taking the calculation procedure of the ILS along the z -axis for example, the first grid point in the negative y -direction located on the boundary is set to be the starting point for each z location. At this velocity point, the distance between the two points (ζ) determines the step size for the autocorrelation calculations, and the corresponding autocorrelation calculation is performed in 1-mm increments until the last grid point reaches the same z value. After that, the next starting point for the autocorrelation calculations is taken to be 1 mm in the positive y -direction from the previous one. The above procedure is repeated in a similar manner with 1-mm increments and stops when the starting point is $y = 0.0$ mm. From now on, the autocorrelation is computed in the negative y -direction. For the starting points where $y > 0.0$ mm, the autocorrelation is computed in 1-mm decrements along the negative y -direction, where the step size is still 1 mm. The calculation procedure of ILS along the z -axis is the same as that along the y -axis, and the autocorrelation is calculated in this way for the following two reasons. Firstly, if the autocorrelation calculations are not reversed for $y > 0.0$ mm, then the required step size will compute values outside the range of the grid point. Second, the same interval of steps must be taken to accurately compare the autocorrelation values in order to analyze various data points in engine flow [14].

As for the smallest eddy scale, the main role of the Kolmogorov scale (L_k) is to dissipate the small-scale kinetic energy via molecular viscosity. Under the assumption that the equilibrium range has been resolved in the current grid spacing, it is possible to define a turbulent Reynolds number (Re_{turb}) to describe the turbulence characteristics on the basis of the large-Reynolds-number flow theory [1, 48]. The turbulence Reynolds number connects the largest and smallest scales via the equation

$$Re_{\text{turb}} = (L_k/L_{\text{ILS}})^{-4/3} \quad (23)$$

where L_{ILS} is the average value of the four ILS components. Re_{turb} can also be calculated as follows:

$$Re_{\text{turb}} = vw' \cdot L_{\text{ILS}}/\nu \quad (24)$$

where vw' is the total velocity fluctuation intensity and ν is the kinematic viscosity of the in-cylinder charge.

In a similar way, the mean-flow Reynolds number is calculated according to

$$Re_{\text{mean}} = VW \cdot L_{\text{clearance}}/\nu \quad (25)$$

where VW is the mean velocity magnitude and $L_{\text{clearance}}$ is the clearance between the piston and the pent roof [11].

5 Results and Analyses

5.1 Validation of LES results

It is necessary to validate the LES results before any further data analysis. At first, qualitative comparison is performed by using the ensemble-averaged 2D velocity field of HTRC in the tumble plane at two representative crank angles (i.e., 120° and 270°CA) obtained by PIV and LES. As shown in Fig. 4, the rectangular region of the flow field in the LES predictions corresponds to the PIV measurements. At 120°CA (Fig. 4a, b), there is a strong annular jet near the intake valves. At the same time, a large-scale tumble motion with its vortex center close to the intake valves has been formed. At 270°CA (Fig. 4c, d), the tumble is compressed by the upward moving piston, and the closed intake valves and the friction dissipation result in the decreased magnitude of the mean velocity. Meanwhile, the tumble center moves to the left side close to the exhaust valves.

Both the velocity magnitude and the vortex center location agree well by comparing the LES and PIV results at the same crank angle. However, there are still some differences in the mean flow structures, especially at 270°CA (see Fig. 4c, d). In order to quantitatively compare the LES and PIV results, the relevance index (RI) proposed by Liu and Haworth [49] is introduced as a metric to quantitatively measure the resemblance between two velocity fields. The variation range of RI is from -1 to 1 . When $RI = 1$, it means that this two

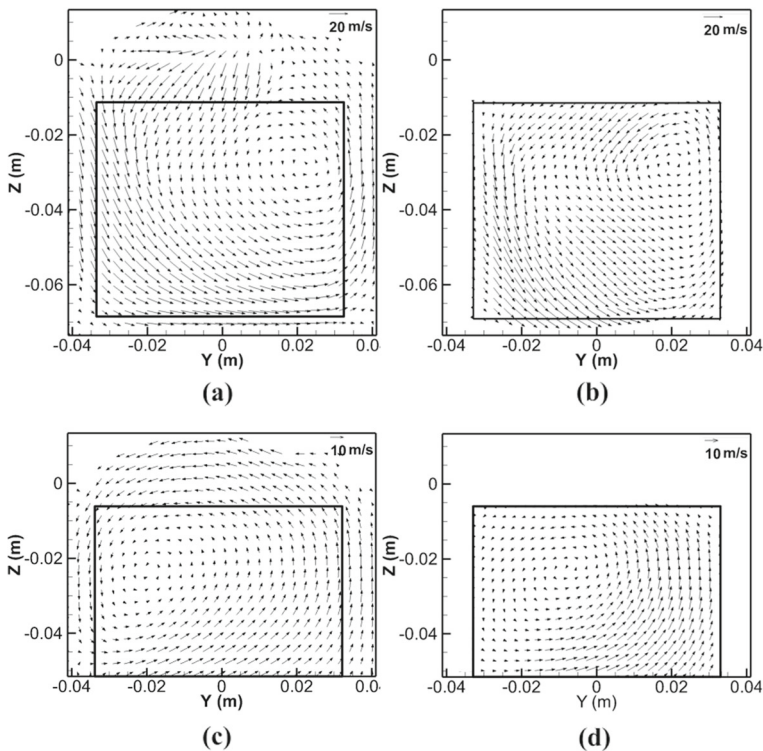


Fig. 4 Ensemble-averaged 2D velocity vectors of HTRC. **a** 120°CA from LES. **b** 120°CA from PIV. **c** 270°CA from LES. **d** 270°CA from PIV

Table 3 Comparison of the relevant index between the experimental and predicted mean/ fluctuating velocity fields

Velocity name	Crank angle degree (°CA)		270°	
	120°	180°	Mean velocity	RMS velocity
HTRC	0.9105	0.9254	0.7938	0.8757
LTRC	0.8622	0.8739	0.7633	0.8749

velocity fields are exactly the same as each other, and when $RI = -1$, it indicates that they have the same velocity magnitude but with the opposite flow direction. When $RI = 0$, it indicates that they are orthogonal, indicating that the two velocity fields are totally different. For the detailed definition, refer to Ref. [39]. The results listed in Table 3 show a high correlation of the mean/RMS velocity fields between LES and PIV.

In order to explore whether the datasets over 60 consecutive cycles are sufficient enough to get the converged results of the mean and RMS velocities, the variations of RI for the mean and RMS velocities of LTRC at five typical phases versus different subsets of cycles are plotted in Fig. 5. In addition, the PIV dataset over 100 consecutive cycles is also

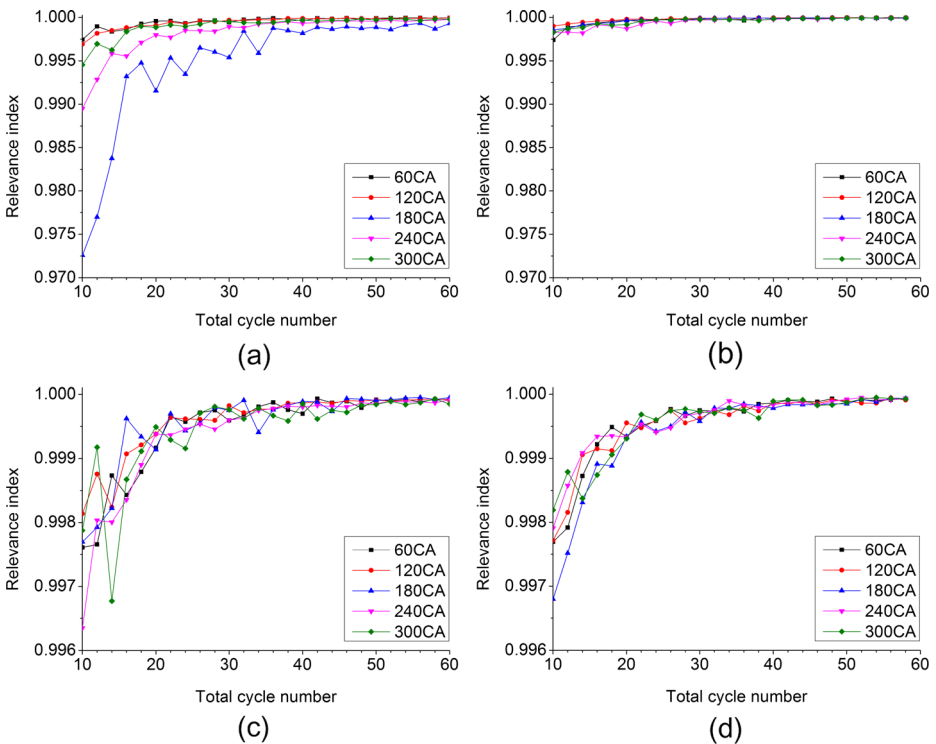


Fig. 5 RI of the mean and RMS velocities for both PIV and LES at different cycle numbers for five different phases in HTRC. **a** Mean velocities measured by PIV. **b** Mean velocities predicted by LES. **c** RMS velocities measured by PIV. **d** RMS velocities predicted by LES

employed to explore the difference between LES and PIV datasets. As known in the previous study [34], the more organized the in-cylinder flow, the less is the number of cycles it needs to get the converged results. As a consequence, it is not necessary to perform the related convergence analysis for HTRC when that of LTRC is analyzed herein. By comparing Fig. 5a with Fig. 5b, it can be concluded that the predicted mean velocities are more stable than the mean velocities measured by PIV over different subsets of cycles. At the same time, the predicted RMS velocities vary less significantly than those of the PIV measurements (see Fig. 5c, d). That implies that the simulation results converge more rapidly than the PIV results. Meanwhile, the CCVs in LES are slightly weaker than those in PIV. Furthermore, the mean and RMS velocities vary insignificantly once the subset of cycles exceeds 40. It suggests that 60 consecutive cycles are ample to get converged results for the mean and RMS velocities at the five typical phases.

In order to quantify the degree of quality of LES, the viscosity ratio [50] (IQ_v) is employed here, and it is defined as

$$IQ_v = \frac{\nu_t}{\nu + \nu_t} \quad (26)$$

where ν_t is the turbulent viscosity and ν is the molecular viscosity.

IQ_v indicates how close the LES is to the DNS limit. To be specific, when $IQ_v = 0$, the current simulation is DNS. As IQ_v decreases, the mesh resolution is finer, and hence, the LES simulation can capture more detailed in-cylinder turbulence characteristics. There is no clear relationship between the value of IQ_v and the mesh resolution required by LES. As indicated by di Mare et al. [50], if IQ_v is below 0.6 to a great extent, most of the energy-relevant structures in the flow field are resolved.

Figure 6 illustrates the spatial distribution of IQ_v according to Eq. 26 in the valve section plane at three different crank angles (i.e., 90°CA, 180°CA, and 270°CA). Both HTRC and LTRC results are shown, and the color scale is identical for all visualizations of this criterion. Based on this quality index, it can be argued that generally, the viscosity ratio in HTRC is higher than that in LTRC. Meanwhile, the mesh resolution is improved to some extent with the globally decreased velocity magnitude during the period from the intake stroke to the compression stroke in both cases. This is also confirmed by the 3D in-cylinder spatially averaged IQ_v listed in Table 4. In addition, it can be found that the strong tumble motion with higher velocity magnitude is adverse to the degree of resolution of turbulent kinetic energy. To be specific, the region in proximity of the intake jets is inadequately resolved to a larger extent compared to the other regions at 90°CA. Hence, the more intense the intake jets, the worse is the grid resolution. Similar results are obtained in the tumble plane.

During compression, the energy-relevant structures in the field are deemed to be mostly resolved when values for IQ_v is smaller than 0.6 in the research of di Mare et al. [50]. As the value of IQ_v in this paper at 270°CA is close or even slightly larger than 0.6, we can draw the conclusion that the grid resolution in our study roughly meets the requirement of LES to get reliable results.

5.2 Flow field analysis

The complex turbulent flow in the cylinder is the basis of all the physical and chemical phenomena in engines and therefore influences the following spray and combustion. As known, a large-scale coherent structure plays an important role in the process of turbulence energy generation and transportation. Therefore, the Q-criterion method [51], which calculates the second-order invariant of the velocity gradient tensor and defines the positive values of this

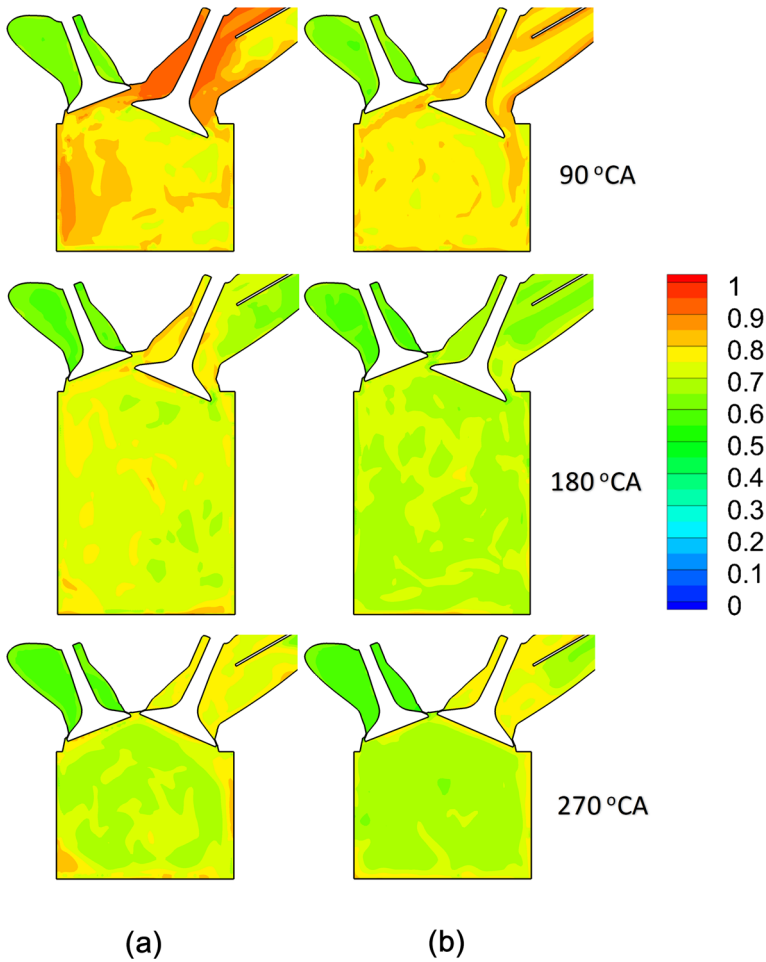


Fig. 6 Comparison of the viscosity ratio in the valve section plane between two cases at three instants. **a** HTRC. **b** LTRC

quantity as vortex regions, is employed here to effectively analyze the evolutions of these large-scale eddies.

Figure 7 shows the predicted transient in-cylinder flow and the corresponding vortex visualization in both cases at three different crank angles on the purpose of better interpreting the impact of the tumble flap on the flow field. It can be seen from Fig. 7a that closing the tumble flap not only forms a single-side intake jet with higher velocity magnitude but

Table 4 Comparison of the in-cylinder spatially averaged viscosity ratio between HTRC and LTRC

Crank angle degree (°CA)	90°	180°	270°
HTRC	0.723	0.671	0.655
LTRC	0.715	0.637	0.630

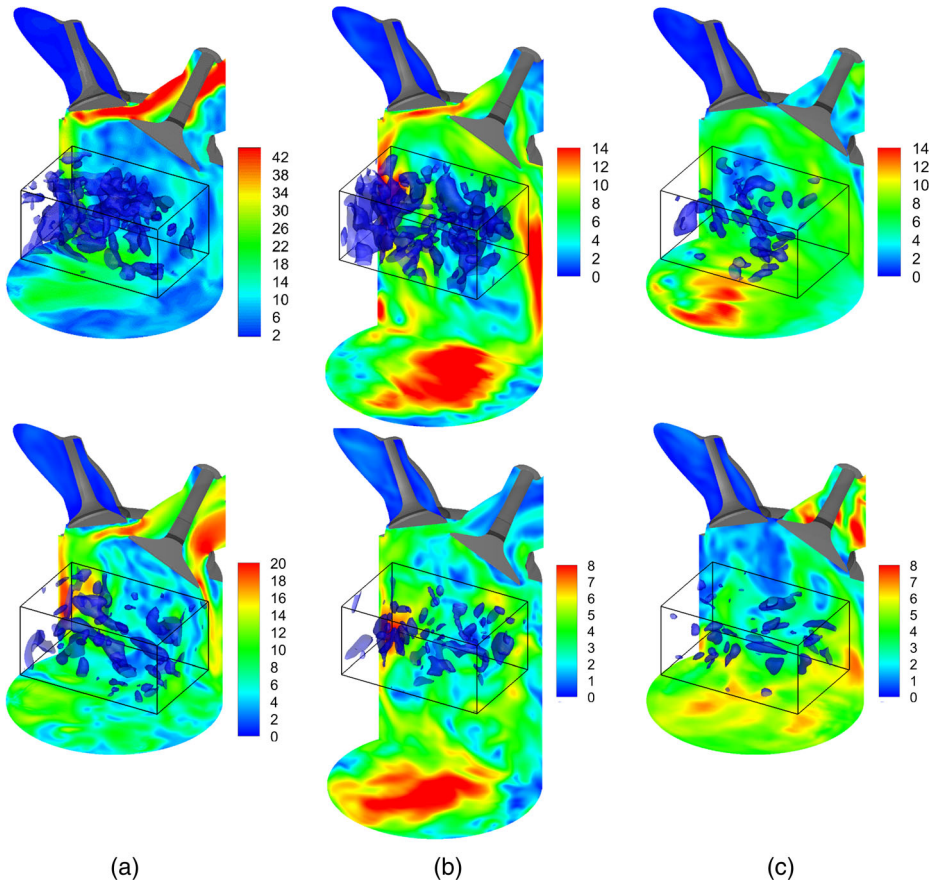


Fig. 7 Comparison of the in-cylinder flow field between HTRC (*upper plots*) and LTRC (*bottom plots*) at three different crank angles: **a** 90°CA ($Q = 1 \times 10^6 \text{ s}^{-2}$), **b** 180°CA ($Q = 2 \times 10^5 \text{ s}^{-2}$), and **c** 270°CA ($Q = 1 \times 10^5 \text{ s}^{-2}$)

also induces stronger coherent structures at the beginning of the intake stroke. Thereafter, the global kinetic energy is decreased and part of the large-scale eddies are damped out with the weakened intake jets (see Fig. 7b). What is more, through the observation of the flow field in the valve section plane and the surface of the piston head, it can be found that the velocity magnitude close to the boundary wall is higher in HTRC than in LTRC, indicating that a tumble motion has already been formed at this moment. After the intake valves are closed, only the upward moving piston provides energy to the in-cylinder air motion. Hence, the velocity magnitude and the intensity of the coherent structures in HTRC are further decreased but still larger than that of LTRC thanks to the surviving tumble towards the end of the compression phase (see Fig. 7c).

In order to analyze the impacts of the tumble flap on velocity fluctuation intensity, the contour maps of the fluctuation intensities corresponding to the three components of the 2D velocity field at 180°CA are plotted in Fig. 8. As seen, the RMS of the Z-component fluctuating velocity is different from that of the Y-component. This means that the RMS of the in-cylinder velocity fields strongly depends on the direction. In addition, the RMS

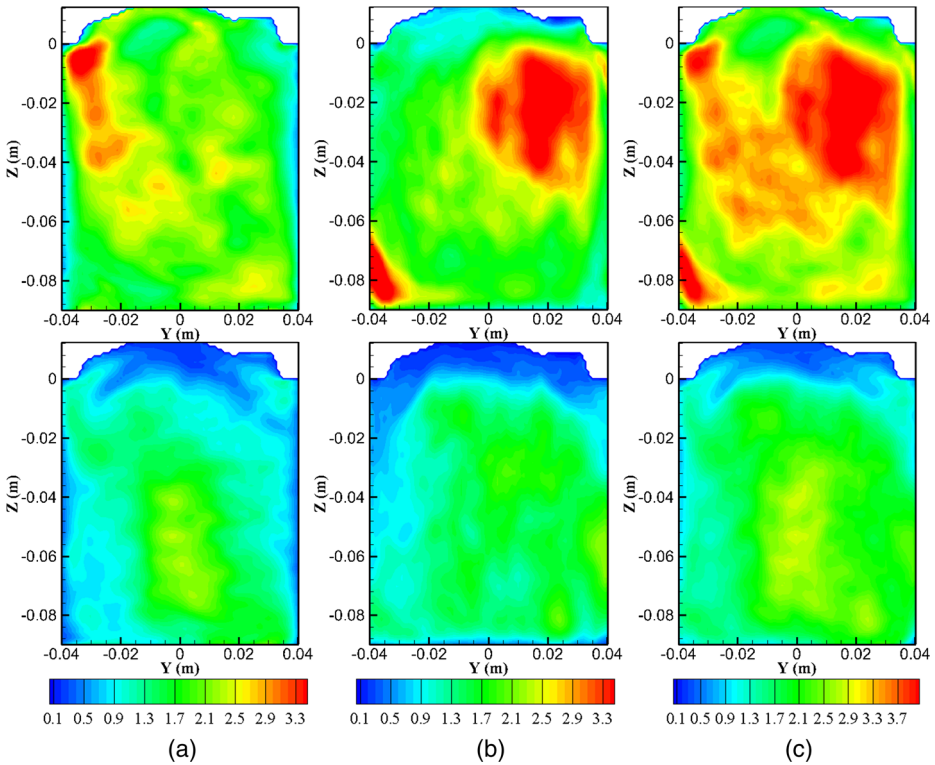


Fig. 8 Comparison of the fluctuation intensities of the in-cylinder velocity fields between HTRC (*upper plots*) and LTRC (*bottom plots*) at 180°CA. **a** *Y*-component fluctuating velocity. **b** *Z*-component fluctuating velocity. **c** Total fluctuating velocity

of the *Z*-component fluctuating velocity dominates the total fluctuation intensities because of the similarity between the RMS of the total fluctuating velocity and the *Z*-component fluctuating velocity.

In regard to the influence of the tumble flap on the velocity fluctuation intensities, it can be observed from Fig. 8 that the closed tumble flap enhances the overall in-cylinder RMS and changes the RMS distribution. Compared to LTRC, a stronger tumble flow with higher RMS in the middle area and near the boundary is formed by HTRC because of the more intense interaction of the intake jets with the wall and the air in the cylinder. By comparing Fig. 8a, the RMS of the *Y*-component fluctuating velocity in HTRC is higher in most area than that in LTRC due to the shearing effects of the tumble bulk flow and the impingement of the intake jets on the cylinder wall. In contrast, the high RMS area of the *Y*-component fluctuating velocity in LTRC is mainly concentrates in the lower middle part of the cylinder due to the interaction of the intake jets from both sides of the intake valves. In addition, the area with higher RMS of the *Z*-component fluctuating velocity attributes to the crash of the upward anticlockwise tumble flow with the downward intake jets for HTRC.

In order to evaluate the impact of the tumble flap on the RMS of the *Y*-component, *Z*-component, and total fluctuating velocities during the entire intake and compression strokes, the comparison of the spatially averaged RMS of the three components of the fluctuating

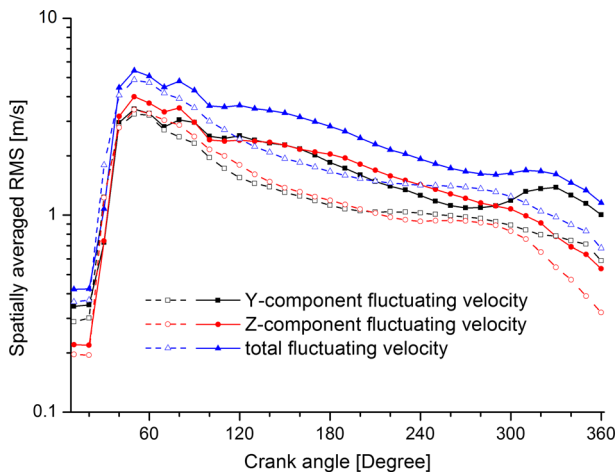


Fig. 9 Comparison of the RMS between HTRC (solid lines + solid symbols) and LTRC (dash lines + open symbols) as a function of the crank angle

velocities between HTRC and LTRC is plotted in Fig. 9. It is observed that all the fluctuating intensities in the two cases increase sharply at the beginning of the intake process and then decrease gradually due to the weakened intake jets and energy dissipation. However, the RMS of the two components in HTRC is higher and more fluctuant than that in LTRC over the entire working process. On the other hand, closing the tumble flap can aggravate the discrepancy of the RMS between the Y - and Z -components since 160°CA . During the late period of the compression stroke, the upward moving piston depresses the fluctuating intensity in the Z -coordinate for both cases. Nevertheless, the more intensive breakdown of the tumble motion in HTRC leads to higher fluctuating intensities since 300°CA , especially in the Y -coordinate. In addition, the stronger tumble motion induced by the closed tumble flap increases the fluctuating kinetic energy during the latter period of the compression phase, while the weaker tumble motion induced by the open tumble flap apparently does not.

Figure 10 illustrates the cyclic variations of the total velocity fluctuation in the Y - and Z -coordinates in both HTRC and LTRC. It can be found that the CCVs of the two components for the total velocity fluctuation are different over the whole period. More specifically, the CCVs of the total velocity fluctuation are larger in HTRC compared to LTRC at the beginning of the intake stroke. Thereafter, the CCV of the total velocity fluctuation in HTRC keeps smaller since about 150°CA under the effect of stronger tumbler motion induced by the closed tumble flap. In other words, the higher tumble is better to reduce CCV. At the end of compression stroke, the CCVs of the total velocity fluctuation in the Y - and Z -coordinates in HTRC increase more sharply but are still lower than that in LTRC because of the more intensive breakdown of the tumble motion. As for the difference of CCV between Y - and Z -coordinates in both cases, it can be observed that the CCVs of the total velocity fluctuation in the Y -coordinate keep larger compared to the one in the Z -coordinate, indicating that the moving piston motion has a positive effect on suppressing the cyclic variations.

5.3 Impacts of the tumble flap on integral length scale and small-scale structure

The description of the in-cylinder turbulence characteristics requires more than just the turbulence fluctuating intensity. A cascade process of eddies generating and dissipating in

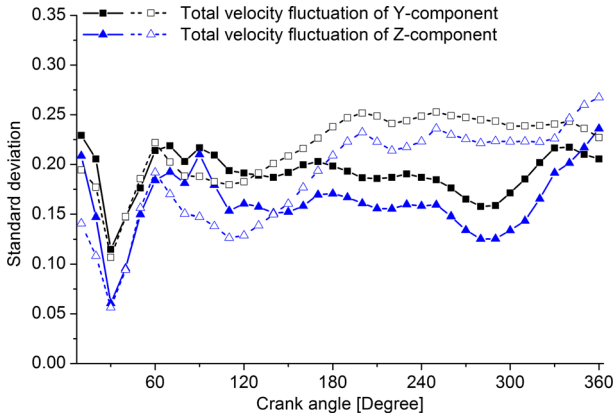


Fig. 10 Relative standard deviations of the total velocity fluctuation for the *Y*- and *Z*-component velocity between HTRC (solid lines + solid symbols) and LTRC (dash lines + open symbols) as a function of the crank angle

different spatial scales exists in a turbulent flow field. Among these eddies with a wide range of length scales, the ILS containing most of the turbulence kinetic energy can effectively identify the size of the largest turbulent eddies. Theoretically, the ILS of low frequency and high frequency and the total velocity fluctuations can be calculated from Eqs. 17 to 22. Nonetheless, the grid spacing is about 1 mm in the present LES simulation, which can resolve the turbulence inertial range, but is not small enough to calculate the high-frequency ILS. On the other hand, the low frequency and total fluctuating velocity are within a similar magnitude and distribution. Hence, the four different ILS components are computed only using the corresponding components of the total fluctuating velocity. It should be noted that the actual ILS of the in-cylinder turbulence is smaller than the ILS calculated using the total fluctuating velocity due to the cyclic variations [11].

The ILS contour maps of the four different components at 180°CA are plotted in Fig. 11. The discontinuity of ILS at $y = 0.0$ mm shown in Fig. 11a, c is due to the fact that the autocorrelation calculations are performed in different directions once the location of the starting point passes through the middle position. Similar situations are for the discontinuity of the horizontal symmetry line of the ILS distribution in the *Z*-coordinate (see Fig. 8b, d). It can be observed from Fig. 11 that all the four ILS components distribute rather differently and randomly. Besides, the ILS components corresponding to the cross-velocity components (i.e., L_{yz} and L_{zy}) are generally smaller than the other ILS components (i.e., L_{yy} and L_{zz}). The above features indicate that the in-cylinder flow field is turbulent, inhomogeneous, and anisotropic at a high degree [11, 52]. On the other hand, by comparing the distributions between ILS and RMS shown in Figs. 8 and 11, it can be found that higher RMS corresponds to larger ILS components, L_{yy} and L_{zz} . It can be deduced that the distribution and magnitude of ILS are affected by velocity fluctuation intensities which can be changed by controlling the ensemble-averaged flow field. This can be confirmed by comparing the ILS contour maps between HTRC and LTRC. Switching the tumble flap which changes the distributions and increases the magnitude of the bulk flow and RMS can further alter the distribution and magnitude of the ILS components, L_{yy} and L_{zz} , to a larger extent compared with the other two components (i.e., L_{yz} and L_{zy}).

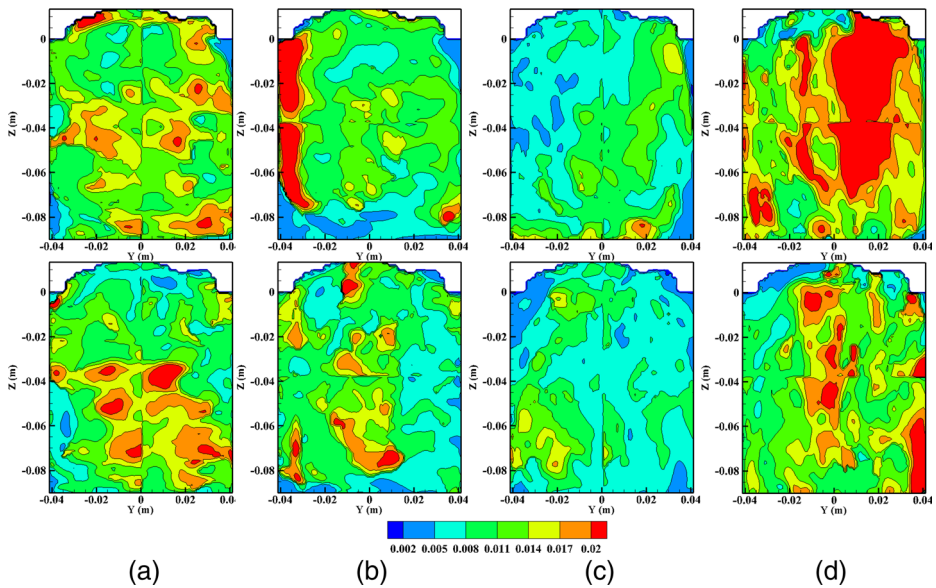


Fig. 11 Distribution of the four ILS components for HTRC (*upper plots*) and LTRC (*bottom plots*) at 180°CA: **a** L_{yy} , **b** L_{yz} , **c** L_{zy} , and **d** L_{zz}

For the purpose of evaluating the impact of the tumble flap on the different ILS components, the evolution of the spatially averaged ILS in the tumble plane is plotted in Fig. 12. It can be seen from Fig. 12a, b that the four ILS components are different from each other except at the beginning of the intake stroke, indicating that the turbulent flow field is anisotropic. The ILS components corresponding to the cross-velocity components (i.e., L_{yz} and L_{zy}) are always smaller than the other two ILS components (i.e., L_{yy} and L_{zz}) over all the available phases. On the other hand, each ILS component is significantly affected by the tumble flap. Closing the tumble flap increases not only L_{zz} with the maximum value of 16.4 mm during the period from 120°CA to 270°CA but also L_{yy} with the maximum value of 16.8 mm during the period from 270°CA to 340°CA, while the variations of L_{yz} and L_{zy} are roughly consistent.

Aiming to further understand the evolution of the ILS, the orthogonal combination of the four ILS components according to Eqs. 21 and 22 is illustrated in Fig. 12c, d. It can be found that in HTRC, the total ILS in Y - and Z -coordinates (L) has a similar pattern with nearly the same largest length over the whole period and is larger than that with LTRC during most of the phases from 120°CA to 280°CA. When the tumble flap is closed, the total ILS in the Y -coordinate (L_y) is depressed while the total ILS in the Z -coordinate (L_z) is strengthened over the phases from 160°CA to 280°CA. It is interesting to find that the total ILS in the Y -coordinate (L_y) increases rapidly for a short time from 280°CA in HTRC, owing to the tumble breakup. The abnormal growth of L_y is mainly resulted from the high fluctuating intensities in the Y -coordinate (see Fig. 9). In the late compression stroke, all the ILS components decrease gradually due to the high-energy dissipation and the reduced cylinder volume caused by the upward moving piston.

Since the strong mean and fluctuation flow has a positive effect on the air–fuel mixing and the fast flame propagation, the influence of the tumble flap on the in-cylinder bulk

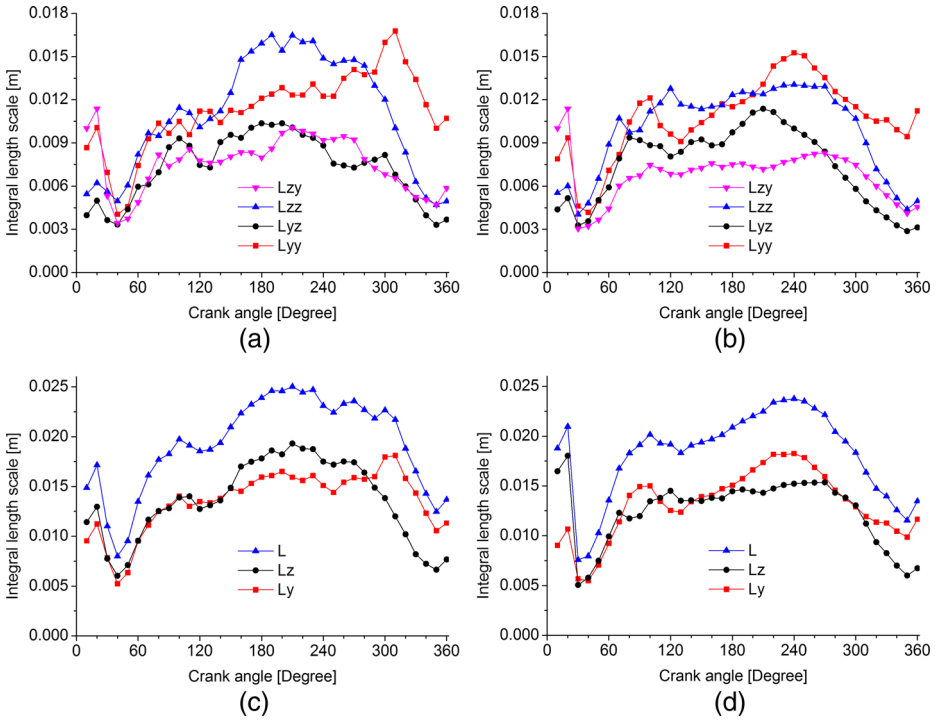


Fig. 12 Spatially averaged ILS during the intake and compression strokes. **a** Four ILS components of HTRC. **b** Four ILS components of LTRC. **c** The total ILS of HTRC in the *Y*- and *Z*-coordinate directions. **d** The total ILS of LTRC in the *Y*- and *Z*-coordinate directions

flow and small-scale structures is further investigated by calculating the mean and turbulent Reynolds numbers. All the following parameters of the turbulence flow are calculated at 330°CA because it is an important moment for the charge-stratified lean-burn combustion. The kinematic viscosity of the in-cylinder charge (ν) is assumed to be $6 \times 10^{-6} \text{ m}^2 \text{ s}^{-1}$, and the clearance between the piston and the pent roof ($L_{\text{clearance}}$) is set to be 0.0176 m. The relevant predicted parameters are listed in Table 5, where the turbulent Reynolds number is calculated according to Eq. 24, the Kolmogorov scale is calculated according to Eq. 23, and the mean Reynolds number is calculated according to Eq. 25.

It can be found that the strengthened tumble motion induced by the closed tumble flap increases both the mean and turbulent Reynolds numbers but decreases the Kolmogorov scale. Thus, it can be expected that closing the tumble flap can promote the following air–fuel mixing and fast-burning process because of the high mean and fluctuation flow and can

Table 5 Mean and turbulent Reynolds numbers and Kolmogorov scales

Case name	Mean velocity (m s^{-1})	Total RMS (m s^{-1})	Mean Reynolds number	Turbulent Reynolds number	Kolmogorov scale (m)
HTRC	3.98	2.1	11,600	2300	2.0×10^{-5}
LTRC	1.86	1.3	5400	1300	2.7×10^{-5}

decrease the kinetic energy dissipation resulting from the small Kolmogorov scale. Nonetheless, as reported by Khalighi [53] and Li et al. [11], the intensity of the in-cylinder tumble flow should be optimized on the purpose of obtaining good turbulence during the combustion process. An excessively strong tumble motion may cause misfire by blowing out the initial flame kernel at the beginning of ignition, especially in charge-stratified lean-burn combustion engines. The predicted mean and turbulent Reynolds numbers and Kolmogorov scale in HTRC are totally consistent with the results of Li et al. [11].

5.4 CCV of tumble ratio and tumble center

As previously mentioned, the in-cylinder flow with tumble motion is more effective to keep and further transfer the kinetic energy generated during the induction stroke to turbulence compared with the one without tumble. At the same time, a stable tumble motion is highly desirable on the purpose of decreasing the CCV, especially during the compression stroke. The fluctuation of the tumble motion under different tumble flap positions is evaluated in this section. The analysis is performed from 230°CA to 320°CA, when the tumble ratio is at a high degree of visual contrast and its fluctuation has a more direct effect on the following fuel injection and combustion process. In order to detect the tumble center precisely, the predictor–corrector scheme [54] is employed. The detailed description of this scheme is given as follows. The streamlines method (as the predictor method) is used first to find the area containing the potential vortex centers, and then the pattern-matching algorithm using the Hamel–Oseen model (as the correction method) is carried out to process the velocity data in the reduced region. To avoid the interference of the small-scale fluctuation velocities, a low-pass filtering procedure is used to process the original velocity fields, and the individual cycle data is ignored in the following calculation if the corresponding instantaneous velocity field does not show a tumble vertex center.

The relative deviation of the tumble ratio and tumble center over phases is depicted by the box and whisker chart (see Fig. 13), which is a convenient way to show the difference among the numerical data without any assumption of the underlying statistical distribution. For the velocity field datasets, the full range and the interdecile range are employed to demonstrate the CCV of the tumble ratio and the tumble center.

As indicated in Fig. 14, the full range and the interdecile range of the tumble ratio in HTRC are smaller than those in LTRC at the same crank angle. Thus, it can be concluded that a higher tumble ratio corresponds to lower CCV of the tumble ratio. It can also be

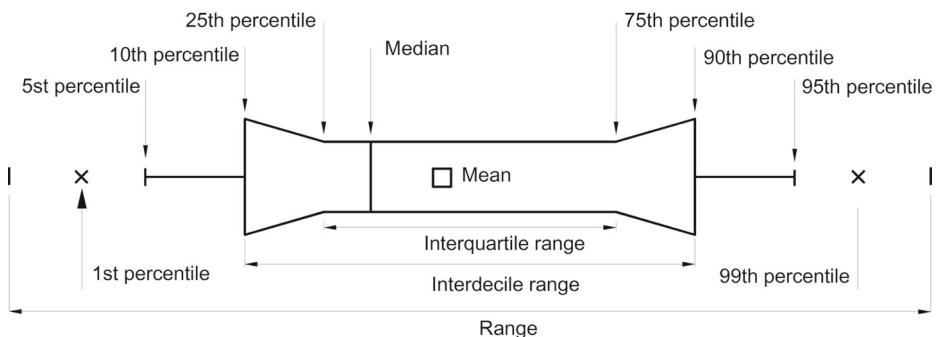


Fig. 13 Values represented in box and whisker chart

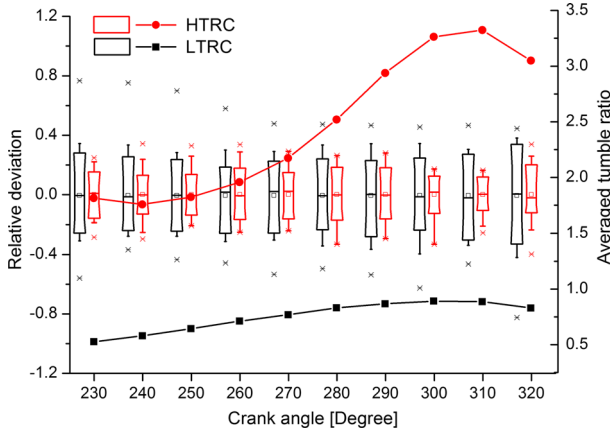


Fig. 14 Relative deviation and the averaged tumble ratio for instantaneous velocity fields of 60 cycles in the tumble plane versus crank angle

found that the magnitude of the tumble ratio shown in Fig. 14 is close to that in Ref. [39], indicating that the flow field characteristics in the tumble plane can reflect the whole in-cylinder flow dynamics approximately. However, there is no direct correlation between the

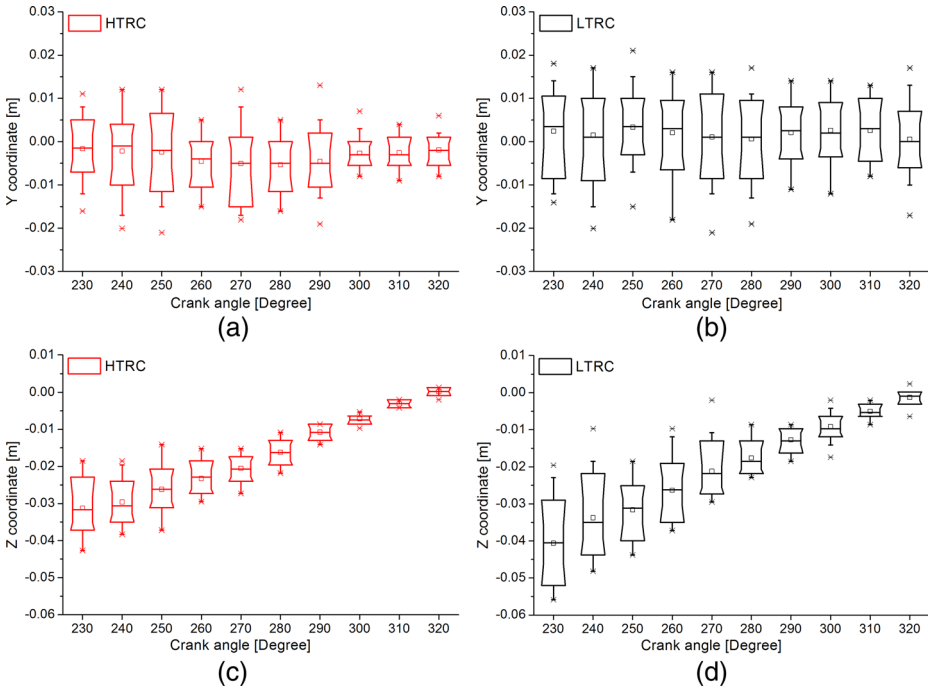


Fig. 15 Cycle-to-cycle variations of the tumble center in the Y- and Z-coordinates for low-pass-filtered velocity fields of 60 cycles. **a** Y-coordinate in HTRC. **b** Y-coordinate in LTRC. **c** Z-coordinate in HTRC. **d** Z-coordinate in LTRC

relative deviation of the tumble ratio and the averaged tumble ratio over phases in each single case through the comparison of the predictions at 240°CA and 320°CA in HTRC.

The CCVs of the tumble center for HTRC and LTRC are depicted in Fig. 15. As presented in Fig. 15a, b, the interdecile range of the *Y*-coordinate in HTRC is smaller than that in LTRC at the same phase. The trend of the interdecile range of the *Y*-coordinate is well consistent with the tumble ratio variation in HTRC, but not in LTRC. As shown in Fig. 15c, d, the interdecile range of the *Z*-coordinate shrinks in both cases as the piston moves up, and the magnitude in HTRC is smaller than that in LTRC at the same phase. The interdecile range of the tumble center is larger in the *Y*-coordinate than that in the *Z*-coordinate, and this feature is consistent with the finding in Ref. [32]. In addition, the upward motion of the piston has a positive effect on re-centering the tumble motion, thus suppressing the fluctuation of the tumble center.

5.5 Analysis of flow decomposition

As mentioned in Section 4.1 (see Eqs. 1 and 2), the triple decomposition of the velocity field can be realized by a 2D spatial low-pass filter by giving a reasonable cutoff length. In this paper, the cutoff length is determined by the spatially averaged ILS for the first time based on the fact that the ILS can effectively estimate the size of the turbulent eddies in the flow, which is generally close to the one of the low-frequency part. In our research, the cutoff spatial scale is set to be 7.90–12.23 mm for HTRC and 8.21–10.54 mm for LTRC over the period from 70°CA to 280°CA, close to that adopted by Liu et al. [32]. Other research studies that used a similar spatial scale can be found in references [11, 30, 55].

Figure 16 presents the results of the FFT triple decomposition at 180°CA in cycle 50. As well known, the inherent edge effects resulting from the 2D FFT increase the large- and small-scale fluctuating velocities abnormally and further affect the calculated turbulence

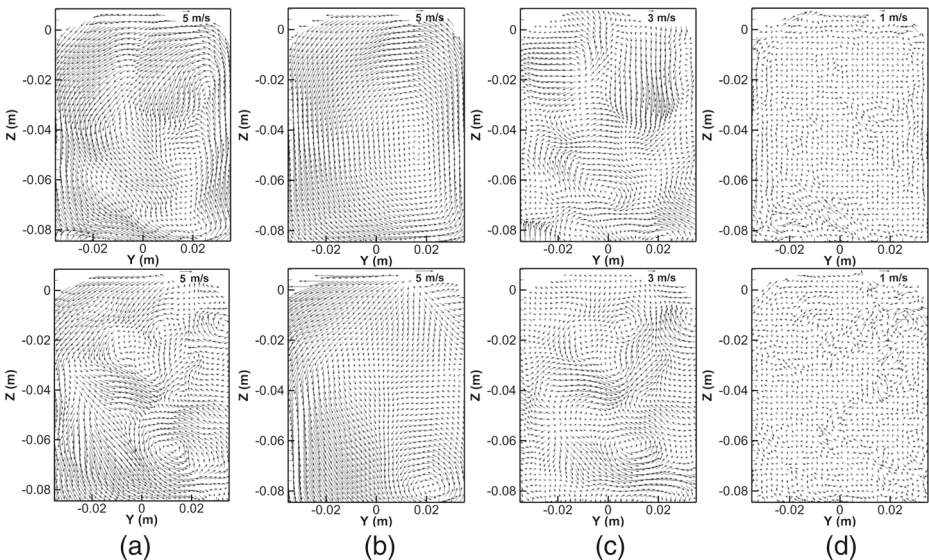


Fig. 16 Comparison of the instantaneous velocity fields and the corresponding subfields of cycle 50 at 180°CA between HTRC (upper plots) and LTRC (bottom plots). **a** Instantaneous velocity field. **b** Ensemble mean part. **c** Low-spatial frequency part. **d** High-spatial frequency

intensity and the kinetic energy in different subfields. In order to reduce the bias, five rows and columns of data around the boundary of the non-zero velocity fields are omitted in the following calculations.

There are obvious differences in the structures of the three subfields between the two cases. The overall length scale in each subfield exhibits typical characteristic scales, which are in proportion to their kinetic energy. The ensemble mean part is similar to the transient velocity field to a larger extent but without fine random vortexes compared with the other two subfields in both cases (see Fig. 16a, b). It should be noted that this subfield is strongly affected by the boundary conditions such as the valve arrangement, the geometry of the combustion chamber and intake ports, and the kinds of charge motion control valve. The low-spatial frequency part shown in Fig. 16c exhibits several vortexes with small size and uneven distribution. For the high-spatial frequency part shown in Fig. 16d, the chaotic distribution with the smallest homogeneous scales and a minor fraction of the fluctuating energy is observed compared to the other two subfields.

It can also be seen from Fig. 16b that the tumble flap affects the original velocity field and the first two subfields considerably. Closing the tumble flap not only increases the velocity magnitude but also helps form a bulk tumble motion with a relatively stable vortex in the center of the cylinder. Moreover, the kinetic energy in the low-spatial frequency part increases as the tumble flap is closed. However, the position of the tumble flap has an insignificant effect on the high-spatial frequency part except that the velocity magnitude is a larger in HTRC as shown in Fig. 16d. This may attribute to the homogeneous and isotropic turbulence in the high-spatial frequency subfield.

To further examine the energy cascade process, the absolute and relative energy distributions of the flow fields of the three parts in the tumble plane are plotted in Fig. 17. All the absolute and relative energies contained in different subfields are calculated without covering the data located in the range of five-grid spacing away from the boundary of the non-zero velocity field. It can be found in Fig. 17a, b that the ensemble part accounts for most of the total kinetic energy (over 70 %), while the high-spatial frequency part occupies the least kinetic energy throughout the full engine cycle. The energy in the ensemble part decreases due to the violent impingement of the intake jets against the piston head and the cylinder wall during the early intake stroke. The energy percentage of the ensemble part increases, whereas the one of the low-spatial frequency part decreases during the middle intake stroke. This may attribute to the fact that the piston moves away from TDC and the intake jets intensify with the increased intake valve lift. During the late intake phase, the energy percentage of the ensemble part falls down again since the intake jet intensity is weakened with the decreased valve lift and the in-cylinder flow field is not yet formed in a bulk tumble motion.

Thereafter, the energy percentage taken by the ensemble part increases due to the strengthened tumble motion by the upward moving piston over the early compression stroke, although the intake jet has a negligible effect on stabilizing the in-cylinder flow field when the intake valve lift decreases to zero. Finally, an evident energy cascade process can be found in both cases during the late compression phase, and the decreasing relative energy of the ensemble mean part corresponds to the increasing relative energy of the low-spatial frequency part. This implies that the compression effect of the piston makes the tumble breakdown and transfers the energy to the following parts by generating coherent structures and small-scale eddies. In addition, the comparison of Fig. 17a with Fig. 17b indicates that closing the tumble flap is capable of suppressing the CCV effectively because the higher the kinetic energy fraction in the ensemble mean subfield, the more organized is the flow field.

It can be seen from Fig. 17c that the total kinetic energy of the three subfields increases rapidly with high-speed air inducted into the cylinder and then decreases gradually due to

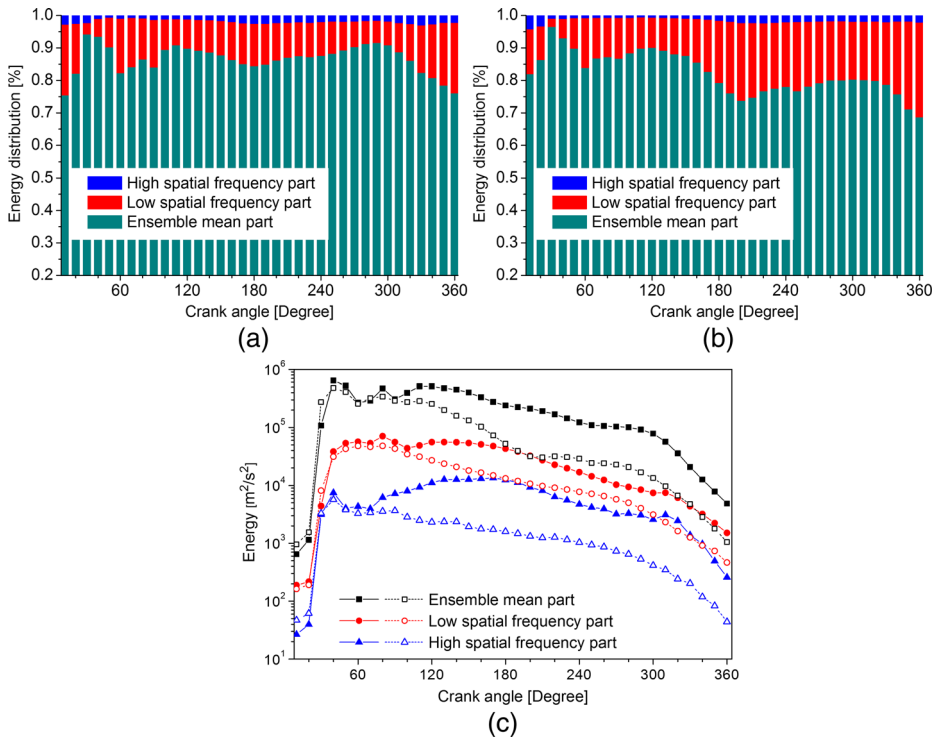


Fig. 17 Comparison of the energy distribution of the three subfields between HTRC (solid lines + solid symbols) and LTRC (dash lines + open symbols) versus crank angle. **a** Relative energy distribution in HTRC. **b** Relative energy distribution in LTRC. **c** Absolute energy distribution

the weakened intake jets and the small-scale energy dissipation via molecular viscosity in both cases. The kinetic energy of all the three subfields is higher in HTRC than in LTRC from about 80°CA to 360°CA. This means that closing the tumble flap is helpful for the generation of a more stable tumble motion by maintaining much more intake jet energy until at TDC compared with the open tumble flap. The intensified tumble breakdown process subsequently releases more turbulent energy, which is finally transferred to the turbulent structures at the smallest scale (i.e., the Kolmogorov scale) in the following ignition and combustion process. As can be expected, a fast-burning combustion with a small CCV will be produced by closing the tumble flap.

5.6 CCV analysis based on 2D FFT

The turbulence in IC engines is strongly unsteady, compressive, rotational, and anisotropic, so that the flow structures and energy transport of in-cylinder turbulent flows are different from those of conventional turbulent flows. The traditional phase-averaging procedure is unable to separate the large- and small-scale flow structures and hence is insufficient for the corresponding CCV analysis. In this section, in-depth investigations on the cyclic variations of in-cylinder turbulence with different spatial scales are conducted using a 2D FFT procedure with the purpose of clarifying the spatial distribution of CCV and find out which part contributes more to the overall CCV. In addition, the influence of the tumble

flap on multi-scale flow structures can also be interpreted better by the virtue of the above procedure.

In order to exhibit the CCV distribution of the low- and high-spatial frequency subfields in the cylinder, the standard deviation of the Y - and Z -component velocity at 180°CA is displayed in Fig. 18. As can be observed from Fig. 18a, b (or Fig. 18c, d), the low-frequency CCVs are generally larger than the high-frequency CCVs in both directions. The distribution of the cyclic variations for the low-spatial frequency part in the Y -coordinate is different from that in the Z -coordinate, indicating that the low-spatial frequency part is anisotropic and inhomogeneous. On the other hand, the RMS distribution shown in Fig. 8 is similar to that of the low-frequency CCV; thus, it can be concluded that higher fluctuation intensity results in larger low-frequency CCV. However, higher fluctuation intensity in HTRC leads to a lower CCV compared with LTRC. Therefore, it is noteworthy that the above conclusion is only valid in the same flow field.

The high similarity of the CCV distribution between the Y - and Z -component velocities in the high-spatial frequency part indicates that the high-spatial frequency part is isotropic and independent of the tumble flap position but not homogeneous. It is also important to notice that the tumble motion induced by the closed tumble flap not only suppresses the CCV but also changes the CCV distributions of the subfields. The CCVs of the high-spatial frequency part are higher in the central area and around the perimeter of the flow field in HTRC. This indicates that the in-cylinder large-scale structures have been stretched, squeezed, and sheared by both of the neighboring flow layers and the boundary wall, leading to small-scale structures with high CCV. Moreover, the area with lower CCV corresponds to stronger bulk flow motion. As shown in Fig. 17c, the tumble motion has a positive effect on lowering the dissipation rate of the kinetic energy of the low- and high-frequency parts.

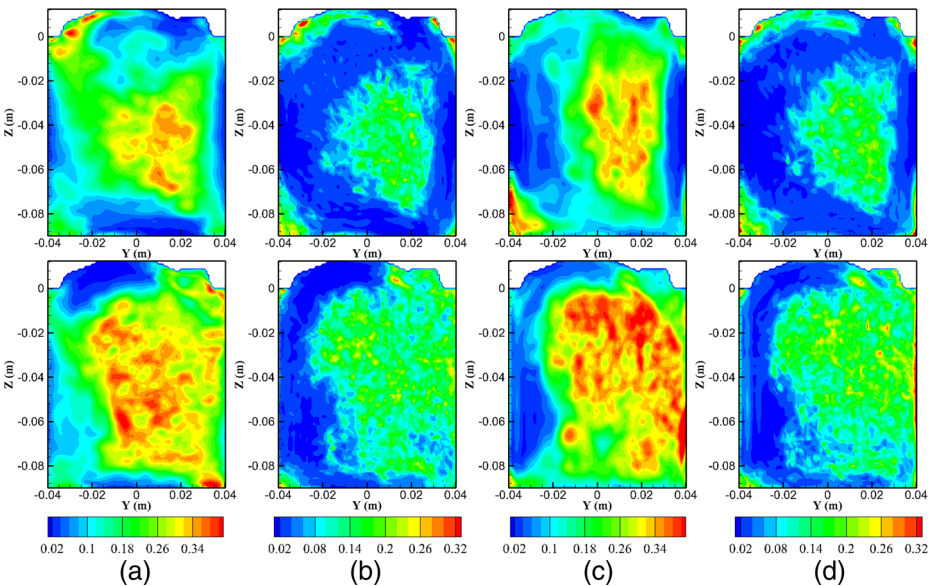


Fig. 18 Comparison of the cycle-to-cycle variations of the low- and high-spatial frequency subfields for the Y - and Z -component velocity between HTRC (*upper plots*) and LTRC (*bottom plots*) at 180°CA . **a** Low-spatial frequency part of the Y -component. **b** High-spatial frequency part of the Y -component. **c** Low-spatial frequency part of the Z -component. **d** High-spatial frequency part of the Z -component

It, therefore, can be concluded that the extent to which the kinetic energy dissipates is proportional to the corresponding CCVs which are in inverse proportion to the ordered degree of the bulk flow effectively.

To quantify the cyclic variations of the low- and high-spatial frequency subfields, the standard deviation of the spatially averaged fluctuating velocity in the *Y*- and *Z*-coordinates is calculated and shown in Fig. 19. As can be seen in this figure, the CCVs of the low-spatial frequency part are larger than those of the high-spatial frequency part over the whole phases. This is consistent with the results of Young [2] and Ozdor et al. [3], in which it was found that the unstable coherent structures containing most of the fluctuating energy may play a dominant role in triggering the cyclic variability. For the CCV dispersion between the *Y*- and *Z*-components, it can be found that the CCV of the high-spatial frequency subfield for the *Y*- and *Z*-components is more consistent compared with that of the low-spatial frequency subfield. This implies that the in-cylinder small-scale flow structures in the high-spatial frequency subfield are mainly isotropic while the large-scale structures which dominate the low-spatial frequency subfield are primarily anisotropic.

Furthermore, closing the tumble flap can effectively decrease the CCV of the low-spatial frequency part to a larger extent from about 120°CA to 300°CA compared with the high-spatial frequency part. It should also be noted that the high-spatial frequency part plays a negligible role in the CCV of the integral flow fields due to its small energy percentage, although the CCVs of the high-spatial frequency part are evident. It is also interesting to find that the stronger tumble flow induced by the closed tumble flap leads to a higher CCV of the low-spatial frequency part for the *Y*-component, which may attribute to the higher RMS of the *Y*-component fluctuating velocity shown in Fig. 9 when the piston moves close to TDC.

The above analyses have proved that the 2D FFT procedure is a useful tool to investigate the effect of the tumble flap on the in-cylinder CCV of each subfield. The results reveal that CCV is mainly generated by large-scale structures in the low-spatial frequency subfield, rather than small-scale structures in the high-spatial frequency subfield. When the tumble flap is closed, a stable tumble motion is formed. It not only suppresses the CCV but also changes the CCV distributions of the low- and high-spatial frequency subfields.

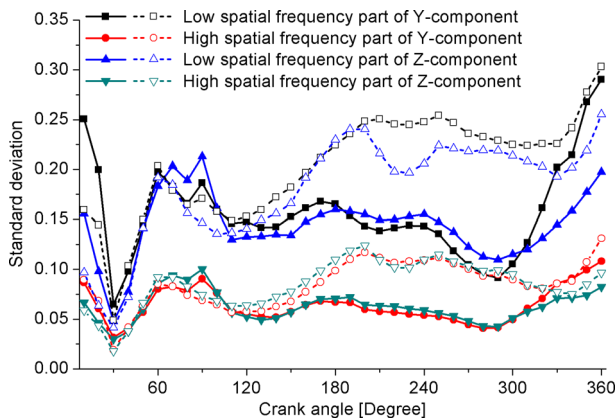


Fig. 19 Relative standard deviations of the low- and high-spatial frequency subfields for the *Y*- and *Z*-component velocity between HTRC (solid lines + solid symbols) and LTRC (dash lines + open symbols) as a function of the crank angle

More specifically, the CCVs of the low-spatial frequency subfield are depressed to a larger extent but still larger than those of the high-spatial frequency subfield under the effect of the strong tumble motion induced by the closed tumble flap. Thus, the in-cylinder aerodynamic dispersions can be adapted and monitored by switching the tumble flap.

6 Conclusions

In this paper, multi-cycle LES is performed to capture the instantaneous in-cylinder turbulent structures in a DISI engine equipped with a specific kind of charge motion control valve named the tumble flap in the intake port. The characteristics of the velocity fluctuation intensity, multi-scale structures, the CCV of the whole flow field, and the large- and small-scale CCV under the effect of the tumble flap are analyzed.

The effects of the tumble flap on the overall in-cylinder flow are firstly discussed. The conclusions are summarized as follows:

1. A single-side intake jet is induced with stronger coherent structures by closing the tumble flap. Besides, the intensified tumble helps maintain the velocity magnitude and the intensity of the coherent structures at a high level towards the end of the compression phase.
2. Closing the tumble flap not only increases the magnitude of the integral length scale (ILS) components in the Z -coordinate during the late intake stroke and the early compression stroke but also forms strong mean and fluctuation flow with the small Kolmogorov scale towards the end of the compression phase.
3. The strong tumble flow induced by the closed tumble flap decreases the CCV of the tumble ratio and the tumble center in the Y - and Z -coordinates and suppresses the fluctuation of the tumble ratio.

Secondly, a newly developed 2D FFT triple decomposition method with the spatially averaged ILS as the cutoff length is employed on the purpose of better interpreting the influence of the tumble flap on multi-scale flow structures. The main results can be summarized as follows:

1. The 2D FFT triple decomposition method is an efficient tool for decomposing an instantaneous velocity field, and choosing the ILS as the cutoff length scale is reasonable.
2. The three subfields of the velocity have their particular characteristic scales of the flow structure while sharing a close relationship with each other. The ensemble mean part accounts for more than 70 % of the total kinetic energy. Switching the tumble flap greatly affects the velocity magnitude and the flow structures of the first two subfields and decreases the rate of energy decay.

Finally, CCV analysis based on the 2D FFT procedure is performed to separate the large- and small-scale flow structures and further investigate the corresponding CCV, respectively, to find out which part contributes more to the overall CCV. The following conclusions are obtained:

1. The high-spatial frequency part is isotropic and independent of the tumble flap position but not homogeneous. Instead, the low-spatial frequency part is isotropic and susceptible to the in-cylinder charge motion.

2. The higher fluctuation intensity leads to the larger CCV of low frequency. The low-spatial frequency part demonstrates a higher CCV compared with the high-spatial frequency part. Closing the tumble flap can effectively suppress the CCV of the low and high-spatial frequency parts.

Acknowledgments The financial supports from the National Natural Science Foundation of China (Grant Nos. 91441111 and 51476151) are gratefully acknowledged.

References

1. Heywood, J.B.: *Internal Combustion Engine Fundamentals*. McGraw-Hill, New York (1988)
2. Young, M.B.: Cyclic dispersion in the homogeneous-charge spark-ignition engine—a literature survey. SAE Technical Paper 810020 (1981)
3. Ozdor, N., Dulger, M., Sher, E.: Cyclic variability in spark ignition engines a literature survey. SAE Technical Paper 940987 (1994)
4. Berkooz, G., Holmes, P., Lumley, J.L.: Low dimensional models of the wall region in a turbulent boundary layer: new results. *Physica D* **58**(1), 402–406 (1992)
5. Wang, T.Y., Liu, D.M., Tan, B.Q., Wang, G.D., Peng, Z.J.: An investigation into in-cylinder tumble flow characteristics with variable valve lift in a gasoline engine. *Flow. Turbul. Combust.* **94**(2), 285–304 (2015)
6. Liu, S.L., Li, Y.F., Lu, M.: Prediction of tumble speed in the cylinder of the 4-valve spark ignition engines. SAE Technical Paper 2000-01-0247 (2000)
7. Liou, T.M., Santavicca, D.A.: Cycle resolved LDV measurements in a motored IC engine. *J. Fluid. Eng-t. Asme.* **107**(2), 232–240 (1985)
8. Fraser, R.A., Bracco, F.V.: Cycle-resolved LDV integral length scale measurements in an IC Engine. SAE Technical Paper 880381 (1988)
9. Fan, L., Reitz, R.D., Trigui, N.: Intake flow simulation and comparison with PTV measurements. SAE Technical Paper 1999-01-0176 (1999)
10. Heim, D., Ghandhi, J.: A detailed study of in-cylinder flow and turbulence using PIV. SAE Technical Paper 2011-01-1287 (2011)
11. Li, Y., Zhao, H., Leach, B., Ma, T., Ladommatos, N.: Characterization of an in-cylinder flow structure in a high-tumble SI engine. *Int. J. Engine Res.* **5**(5), 375–400 (2004)
12. Baumann, M., Mare, F., Janicka, J.: On the validation of large eddy simulation applied to internal combustion engine flows. Part II: numerical analysis. *Flow. Turbul. Combust.* **92**(1-2), 299–317 (2014)
13. Vermorel, O., Richard, S., Colin, O., Angelberger, C., Benkenida, A., Veynante, D.: Towards the understanding of cyclic variability in a spark ignited engine using multi-cycle LES. *Combust. Flame.* **156**(8), 1525–1541 (2009)
14. Funk, C., Sick, V., Reuss, D.L., Dahm, W.: Turbulence properties of high and low swirl in-cylinder flows. SAE Technical Paper 2002-01-2841 (2002)
15. Akkerman, V., Ivanov, M., Bychkov, V.: Turbulent flow produced by piston motion in a spark-ignition engine. *Flow. Turbul. Combust.* **82**(3), 317–337 (2009)
16. Li, Y., Zhao, H., Peng, Z., Ladommatos, N.: Particle image velocimetry measurement of in-cylinder flow in internal combustion engines-experiment and flow structure analysis. *P. I. Mech. Eng. D-j. Aut* **216**(1), 65–81 (2002)
17. Jebamani, R.D., Kumar, T.M.N.: Studies on variable swirl intake system for DI diesel engine using computational fluid dynamics. *Therm. Sci.* **12**(1), 25–32 (2008)
18. Dembinski, H., Ångström, H.: An experimental study of the influence of variable in-cylinder flow, caused by active valve train, on combustion and emissions in a diesel engine at low lambda operation. SAE Technical Paper 2011-01-1830 (2011)
19. Fischer, J., Velji, A., Spicher, U.: Investigation of cycle-to-cycle variations of in-cylinder processes in gasoline direct injection engines operating with variable tumble systems. SAE Technical Paper 2004-01-0044 (2004)
20. Adomeit, P., Jakob, M., Pischinger, S., Brunn, A., Ewald, J.: Effect of intake port design on the flow field stability of a gasoline DI engine. SAE Technical Paper 2011-01-1284 (2011)

21. Bertsson, A.W., Josefsson, G., Ekdahl, R., Ogink, R., Grandin, B.: The effect of tumble flow on efficiency for a direct injected turbocharged downsized gasoline engine. SAE Technical Paper 2011-24-0054 (2011)
22. Ramajo, D., Zanotti, A., Nigro, N.: In-cylinder flow control in a four-valve spark ignition engine: numerical and experimental steady rig tests. P. I. Mech. Eng. D-j. Aut **225**(6), 813–828 (2011)
23. Vu, T.T., Guibert, P.: Proper orthogonal decomposition analysis for cycle-to-cycle variations of engine flow. Effect of a control device in an inlet pipe. Exp. Fluids. **52**(6), 1519–1532 (2012)
24. Barlow, R.S.: Laser diagnostics and their interplay with computations to understand turbulent combustion. P. Combust. Inst. **31**(1), 49–75 (2007)
25. Jiang, X., Siamas, G., Jagus, K., Karayiannis, T.: Physical modelling and advanced simulations of gas-liquid two-phase jet flows in atomization and sprays. Prog. Energy. Combust. **36**(2), 131–167 (2010)
26. Jagus, K., Jiang, X.: Large eddy simulation of diesel fuel injection and mixing in a HSDI engine. Flow. Turbul. Combust. **87**(2-3), 473–491 (2011)
27. Bottone, F., Kronenburg, A., Gosman, D., Marquis, A.: Large eddy simulation of diesel engine in-cylinder flow. Flow. Turbul. Combust. **88**(1-2), 233–253 (2011)
28. Bottone, F., Kronenburg, A., Gosman, D., Marquis, A.: The numerical simulation of diesel spray combustion with LES-CMC. Flow. Turbul. Combust. **4**, 651–673 (2012)
29. Enaux, B., Granet, V., Vermorel, O., Lacour, C., Thobois, L., Dugué, V., Poinot, T.: Large eddy simulation of a motored single-cylinder piston engine: numerical strategies and validation. Flow. Turbul. Combust. **86**(2), 153–177 (2010)
30. Reuss, D.L.: Cyclic variability of large-scale turbulent structures in directed and undirected IC engine flows. SAE Technical Paper 2000-01-0246 (2000)
31. Joo, S., Srinivasan, K., Lee, K., Bell, S.: The behaviour of small-and large-scale variations of in-cylinder flow during intake and compression strokes in a motored four-valve spark ignition engine. Int. J. Engine Res. **5**(4), 317–328 (2004)
32. Liu, D., Wang, T., Jia, M., Wang, G.: Cycle-to-cycle variation analysis of in-cylinder flow in a gasoline engine with variable valve lift. Exp. Fluids. **53**(3), 585–602 (2012)
33. Lumley, J.L.: The structure of inhomogeneous turbulent flows. Atmospheric turbulence and radio wave propagation, pp. 166–178 (1967)
34. Liu, K., Haworth, D.C., Yang, X., Gopalakrishnan, V.: Large-eddy simulation of motored flow in a two-valve piston engine: POD analysis and cycle-to-cycle variations. Flow. Turbul. Combust. **91**(2), 373–403 (2013)
35. Abraham, P., Liu, K., Haworth, D., Reuss, D., Sick, V.: Evaluating large-eddy simulation (LES) and high-speed particle image velocimetry (PIV) with phase-invariant proper orthogonal decomposition (POD). Oil Gas. Sci. Technol. (2013)
36. Chen, H., Reuss, D.L., Hung, D.L., Sick, V.: A practical guide for using proper orthogonal decomposition in engine research. Int. J. Engine Res. **14**(4), 307–319 (2012)
37. Chen, H., Reuss, D.L., Sick, V.: On the use and interpretation of proper orthogonal decomposition of in-cylinder engine flows. Meas. Sci. Technol. **23**(8), 085302 (2012)
38. Roudnitzky, S., Druault, P., Guibert, P.: Proper orthogonal decomposition of in-cylinder engine flow into mean component, coherent structures and random Gaussian fluctuations. J. Turbul. N70 (2006)
39. Wang, T., Li, W., Jia, M., Liu, D., Qin, W., Zhang, X.: Large-eddy simulation of in-cylinder flow in a DISI engine with charge motion control valve: proper orthogonal decomposition analysis and cyclic variation. Appl. Therm. Eng. **75**, 561–574 ((2015))
40. CONVERGE™: A three-dimensional computational fluid dynamics program for transient flows with complex geometries. Convergent Science Inc, Middleton (2009)
41. Speziale, C.: Analytical methods for the development of Reynolds-stress closures in turbulence. Annu. Rev. Fluid. Mech. **23**(1), 107–157 (1991)
42. Werner, H., Wengle, H.: Large-eddy simulation of turbulent flow over and around a cube in a plate channel. In: Durst, F., Friedrich, R., Launder, B.E., Schmidt, F.W., Schumann, U. (eds.) Turbulent shear flows 8, pp. 155–168. Springer, Heidelberg (1993)
43. Goryntsev, D., Sadiki, A., Klein, M., Janicka, J.: Large eddy simulation based analysis of the effects of cycle-to-cycle variations on air-fuel mixing in realistic DISI IC-engines. P. Combust. Inst. **32**(2), 2759–2766 (2009)
44. Yang, X., Gupta, S., Kuo, T.-W., Gopalakrishnan, V.: RANS and large eddy simulation of internal combustion engine flows—a comparative study. J. Eng. Gas. Turb. Power **136**(5), 051507 (2014)
45. Kuo, T.-W., Yang, X., Gopalakrishnan, V., Chen, Z.: Large eddy simulation (LES) for IC engine flows. Oil Gas. Sci. Technol. **69**(1), 61–81 (2014)
46. Fansler, T., French, D.: Cycle-resolved laser-velocimetry measurements in a reentrant-bowl-in-piston engine. SAE Technical Paper 880377 (1988)

47. Li, Y., Zhao, H., Ladommatos, N.: Analysis of large-scale flow characteristics in a four-valve spark ignition engine. *P. I. Mech. Eng. C-j. Mec* **216**(9), 923–938 (2002)
48. Reuss, D., Adrian, R., Landreth, C., French, D., Fansler, T.: Instantaneous planar measurements of velocity and large-scale vorticity and strain rate in an engine using particle-image velocimetry. *SAE Technical Paper 890616* (1989)
49. Liu, K., Haworth, D.C.: Development and assessment of POD for analysis of turbulent flow in piston engines. *SAE Technical Paper 2011-01-0830* (2011)
50. di Mare, F., Knappstein, R., Baumann, M.: Application of LES-quality criteria to internal combustion engine flows. *Comput. Fluids*. **89**, 200–213 (2014)
51. Hunt, J.C.R., Wray, A.A., Moin, P.: Eddies, streams, and convergence zones in turbulent flows. *Center for Turbulence Research* **1**, 193–208 (1988)
52. Pope, S.B.: *Turbulent Flow*. Cambridge University Press, Cambridge (2000)
53. Khalighi, B.: Study of the intake tumble motion by flow visualization and particle tracking velocimetry. *Exp. Fluids*. **10**(4), 230–236 (1991)
54. Vollmers, H.: Detection of vortices and quantitative evaluation of their main parameters from experimental velocity data. *Meas. Sci. Technol.* **12**(8), 1199–1207 (2001)
55. Rouland, E., Trinite, M.: Particle image velocimetry measurements in a high tumble engine for in-cylinder flow structure analysis. *SAE technical paper 972831* (1997)